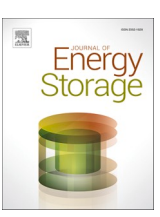
ELSEVIER

Contents lists available at ScienceDirect

Journal of Energy Storage

journal homepage: www.elsevier.com/locate/est



Research Papers

The soluble lead flow battery: Image-based modelling of porous carbon electrodes

Check for updates

E.J. Fraser*, J.P. Le Houx1, L.F. Arenas2, K.K.J. Ranga Dinesh, R.G.A. Wills

Energy Technology Research Group, Faculty of Engineering and Physical Sciences, University of Southampton, Southampton SO17 1BJ, United Kingdom

ARTICLE INFO

Keywords: Image-based modelling Reticulated vitreous carbon Soluble lead flow battery Redox flow batteries Energy storage Porous electrodes

ABSTRACT

A novel numerical modelling framework coupling physics-based model equations and image-based input parameters is developed to simulate the behaviour of the soluble lead flow battery when reticulated vitreous carbon (RVC) electrodes are used. Experimental results are presented to validate the model. Open-source software OpenImpala is used to predict the macro-homogeneous properties of RVC from computed tomography scans of various grades of RVC. The process is repeated on manipulated datasets where a voxel dilation technique has been used to estimate the geometry of RVC electrodes with a range of thicknesses of electrodeposited material. The model predicts that with a region of free electrolyte dividing the electrodes, the electrolyte velocity is low within the electrodes. This is exacerbated by a build-up of deposit close to the inlet. By dividing the electrodes with only a porous separator, a deposit build-up is no longer seen, and the concentration within the electrodes is shown to be far more even. Finally, with an applied current density of 50 mA cm⁻², the overpotential is predicted to be reduced by over 100 mV when 100 ppi RVC electrodes are used instead of 10 ppi electrodes. An experimentally validated voltage efficiency of over 80% is achieved.

1. Introduction

With the increased adoption of intermittent electricity generation at the expense of traditional synchronous generation, the demand for energy storage is growing [1]. A recent study by Homan et al. has shown that the standard deviation of the Great Britain grid frequency has increased significantly since 2014 [2]. This increase is correlated with a growth in renewable energy penetration such as solar and wind. However, the intermittent nature of renewable energy indicates that a combination of different technologies will be required for electricity networks to remain stable. Battery energy storage is likely to play a significant role to tackle the intermittent nature of renewable electricity generation and utilisation [1]. Although lithium-ion batteries provide the majority of battery energy storage currently installed globally [3], decoupling, or partial decoupling, of energy and power, means redox flow batteries (RFBs) can have a lower environmental impact [4] and may be more economical for high energy applications [5].

While vanadium redox flow batteries (VRFBs) provide the vast majority of installed RFB capacity [3], other technologies [6], such as the

soluble lead flow battery (SLFB), provide significant advantages over the VRFB. Lead has an existing supply chain, and it has been proposed that the SLFB can fit into the current recycling system [7,8]. The SLFB can also operate in an undivided configuration, removing the substantial cost of a membrane or microporous separator [9] and has a higher discharge cell potential than the VRFB [10]. Moreover, this chemistry has been subject to continued interest and research for nearly two decades, has achieved high cyclability [11,12] and has been investigated at pre-pilot scale [10].

The main electrode reactions involved in the SLFB are:

Positive:

$$Pb^{2+} + 2H_2O \rightleftharpoons PbO_2 + 4H^+ + 2e^- E^0 = +1.46 \text{ V vs SHE}$$
 (1.1)

Negative:

$$Pb^{2+} + 2e^{-} \rightleftharpoons Pb \ E^{0} = -0.13 \ V \ vs \ SHE$$
 (1.2)

 $^{^{\}star}$ Corresponding author.

E-mail addresses: e.j.fraser@soton.ac.uk (E.J. Fraser), rgaw@soton.ac.uk (R.G.A. Wills).

¹ Current address: Diamond Light Source, Diamond House, Harwell Science and Innovation Campus, Fermi Ave, Didcot OX11 0DE, United Kingdom.

² Current address: Institut für Chemische und Elektrochemische Verfahrenstechnik - Forschungszentrum Energiespeichertechnologien, Technische Universität Clausthal, Goslar 38640, Germany.

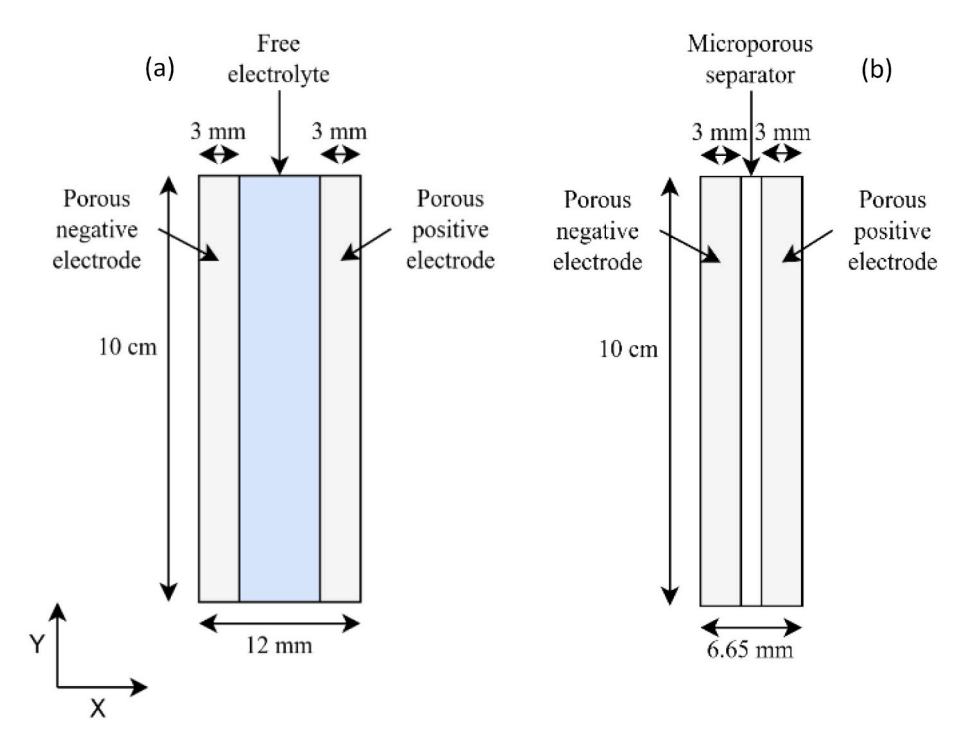


Fig. 1. Schematic showing the geometry used to model the battery. (a) Electrolyte domain divided. (b) Microporous separator divided.

Cell:

$$2Pb^{2+} + 2H_2O \rightleftharpoons Pb + PbO_2 + 4H^+ E_{cell}^0 = +1.59 V$$
 (1.3)

where solid Pb is deposited at the negative electrode and solid PbO $_2$ is deposited at the positive electrode during the charging process. During discharge, both solid deposits are dissolved back into the electrolyte as Pb 2 + ions.

The SLFB contains a two-step charging voltage profile from the second charge onwards, which is associated with the positive electrode. It has been proposed that there is a reversible side reaction where PbO_2 is only partially reduced to Pb^{2+} during discharge, forming a solid PbO_x with x<2 [13]. Shah et al. [14] propose a simplification of this side reaction to:

$$PbO + H_2O \rightleftharpoons PbO_2 + 2H^+ + 2e^- E^0 = +0.28 \text{ V vs SHE}$$
 (1.4)

This side reaction has been adopted in many subsequent SLFB models [15–19].

Indeed, numerical simulation has been a valuable tool in the development of the SLFB, mainly through understanding the current distribution and its relation to the location of deposits. For instance, early work by Pletcher et al. [13] demonstrated a negative correlation between current density and coulombic efficiency in the initial cell design. However, simulations of the SLFB have shown that the low reversibility of the positive electrode reaction can be mitigated by increasing the effective electrode area at the positive electrode; the overpotential of the cell is decreased significantly due to the decrease in local current density [18,20].

Oury et al. [20] investigated the combination of a honeycombshaped positive electrode and two planar negative electrodes. Although the 3D electrode offers a larger surface area, they found that the positive current distribution is heavily reliant on the thickness of the honeycomb, with a higher current occurring at the edges of the channels. Shorter channels gave a more homogeneous current distribution but reduced the electrode area, thereby increasing the average current density. Two cells share a positive electrode in this arrangement, making it impossible to arrange them into a bipolar stack. The monopolar stacks required to use this concept are too expensive for further development.

Nandanwar and Kumar [18] have shown that using concentric cylindrical electrodes with a positive outer substantially decreases the overpotential of the positive electrode, improving the voltage and hence energy efficiency. Energy efficiency was improved from 66% with planar electrodes to 80% using cylindrical electrodes. However, cylindrical and tubular flow cells are notoriously difficult to scale up as bipolar configurations are not possible. High productivity can only be achieved by connecting a large number of individual cells, which demand more material and take up more space.

A bipolar stack is clearly advantageous due to the reduced complexity, more even current distribution and increased space efficiency [21]. An increased electrode area, particularly at the positive electrode, has been shown experimentally and theoretically to be advantageous in the SLFB [10], yet the two previously simulated arrangements (honeycomb and tubular electrodes) have issues when considering scale-up. On the other hand, a number of experimental studies have shown the effectiveness of reticulated vitreous carbon (RVC) as an electrode material [22–26]. RVC electrodes can be combined with a conventional bipolar plate for use in the SLFB.

RVC has good chemical stability, high volumetric porosity and high permeability, making it useful for electrochemical flow cells [27]. RVC is commercially manufactured in a number of different grades ranging from 10 ppi to 100 ppi (pores per inch). It can also act as a coarse scaffold for deposition lead (Pb) and lead dioxide (PbO₂), giving structural rigidity to the electrodes and increasing the surface area [23,24]. This may allow for a greater thickness of electrode deposits, increasing the capacity of the SLFB for a given electrode area. Carbon felts, which are often used in other flow batteries, e.g. the VRFB, are unsuitable for use in the SLFB because the small pores in the material would quickly become blocked with deposited Pb or PbO₂.

Our previous paper highlighted the effect of deposit growth in a high capacity SLFB [28]. Here, a similar methodology is used to numerically model and simulate an SLFB with porous RVC electrodes. In our previous work, the geometry of the reaction chamber changed during charge and discharge with the formation of Pb and PbO $_2$ deposits. However, in this study, a fixed geometry is employed, and the RVC electrodes are

 Table 1

 Source terms for each species in porous electrode reactions.

Species	Source term/mol m ⁻³ s ⁻¹		
	Positive electrode	Negative electrode	
Pb ²⁺	$S_{pb^{2+}}=rac{i_{ u}}{nF}$	$S_{Pb^{2+}} = -\frac{i_{\nu}}{nF}$	
H^+	$S_{H^+} = -\frac{4i_{\nu}}{nF}$	N/A	
Pb	N/A	$S_{Pb} = \frac{i_{\nu}}{nF}$	
PbO_2	$S_{PbO_2} = -\frac{i_{\nu}}{nF}$	N/A	
PbO	$egin{array}{ll} S_{PbO_2} &=& -rac{i_ u}{nF} \ S_{PbO} &=& rac{i_ u}{nF} \end{array}$	N/A	

modelled as a single porous domain with changing porosity, tortuosity, and permeability as a function of state of charge.

The objective of this study is to propose a novel numerical modelling framework to simulate the characteristics of SLFB with the presence of RVC electrodes. Physical properties of RVC electrodes are derived using image-based computer tomography data. Physics-based modelling with electrode parameters derived from tomographic image analysis provides a novel modelling framework to simulate SLFB performance when using RVC electrodes. The paper is organised as follows. Section 2 describes the experimental setup for validating the model; Section 3 discusses the model setup, including governing equations, numerical details, and input data from tomography is presented in Section 4. Section 5 provides results and discussion, followed by conclusions.

2. Experimental setup

Experiments for validating the model were carried out in a flow cell with 4 cm \times 2.5 cm electrodes. This cell consisted of acrylic flow frames, 1.5 mm (uncompressed) silicone foam gaskets, SGL carbon sigracell bipolar plates [29], 5 mm, 80 ppi RVC electrodes divided by an AmerSil FF60 microporous separator, copper foil current collectors, an insulating layer of hard norprene and 10 mm thick stainless steel endplates. The cell was held together with four M8 bolts, one in each corner. This also provided compression to maintain good contact between the RVC and the carbon-polymer plates. 400 cm³ of electrolyte was circulated at a volumetric flow rate of 7 cm³ s $^{-1}$, corresponding to an average electrolyte velocity of approximately 2.3 cm s $^{-1}$ over plain bipolar pates.

trolyte velocity of approximately 2.3 cm s⁻¹ over plain bipolar pates.

The electrolyte consisted of 1.0 mol dm⁻³ methanesulfonic acid and 0.7 mol dm⁻³ lead methanesulfonate. Each cycle consisted of a charge for 1 h followed by discharging until a 0.7 V cut-off voltage. Between each step, the cell was left at open circuit for 120 s.

3. Model setup

In this study, two configurations of the cell were used with slightly different geometry. Fig. 1 shows the geometry used in both configurations: Fig. 1(a) shows the undivided configuration, which includes two porous electrode domains separated by a 6 mm free electrolyte domain, and Fig. 1(b) shows the divided configuration, which replaces the electrolyte domain with a microporous separator domain. The undivided configuration is similar to previous experimental studies that use RVC [22,25,26]. However, the divided configuration is suggested in this study as an alternative for improved cell performance. In a stack, this unit cell of a negative porous electrode, an electrolyte/separator domain, and a positive porous electrode would be divided by bipolar plates with a current collector at either end of the stack. Neither the bipolar plate nor the current collectors are explicitly modelled; the boundary conditions simply imply their presence. The electrical resistance of these components and the interface between the plate and the RVC electrodes are expected to be small.

3.1. Governing equations

In the free electrolyte domain, the flow is assumed to be laminar. The electrolyte velocity, u in m s⁻¹, is therefore described with the laminar form of the Navier-Stokes and continuity equations.

$$\rho \frac{\partial u}{\partial t} + \rho(u \bullet \nabla)u = \nabla \bullet [-p + \mu \nabla u]$$
(3.1)

$$\nabla \bullet u = 0 \tag{3.2}$$

where ρ is the electrolyte density in kg m⁻³, p is pressure in Pa, and μ is dynamic viscosity in Pa s.

In previous models of the SLFB, there have been examples which use fixed values for density and viscosity [14,18-20] and examples which vary the parameters for viscosity or density with concentration [15–17]. Where fixed values are used, the properties of water are typically taken. However, Krishna et al. [30] show that over the expected concentration range (0–0.7 mol dm⁻³ Pb²⁺, 1–2.4 mol dm⁻³ H⁺), density and viscosity of the electrolyte vary substantially with electrolyte concentration (\sim 1–1.3 g cm⁻³ and \sim 1.2–2 mPa s respectively) and differ significantly from those properties of water (1 g cm⁻³ and 0.96 mPa s respectively). As concentration gradients are expected in the porous electrodes, different values of density and viscosity are expected in the electrodes and the bulk electrolyte. As seen in Eq. (3.1), density and dynamic viscosity are important terms when calculating the flow of electrolyte, with a higher density increasing the inertia of the solution and higher viscosity increasing the pressure drop within the cell. Using Krishna et al.'s measurements, [30], viscosity in mPa s, μ_e , is related to concentrations, c, in mol dm⁻³ by Eq. (3.3) and electrolyte density in kg dm⁻³, ρ_e , is related to concentration in mol dm^{-3} by Eq. (3.4).

$$\mu_e = 0.96 + 0.364 \bullet c_{PbII} + 0.407 \bullet c_{PbII}^2 + 0.262 \bullet c_H$$
 (3.3)

$$\rho_e = 1.0 + 0.3 \bullet c_{PbII} + 0.03 \bullet c_H \tag{3.4}$$

In the porous domains (RVC electrodes), the fluid flow is described using the Brinkman equations. These are an extension of Darcy's law, which includes energy dissipation due to viscous shear forces, similar to Navier-Stokes but in porous media. The Brinkman equations become relevant at higher flow rates and are valid at high porosity [31]:

$$\frac{1}{\varepsilon}\rho\frac{d\mathbf{u}}{dt} + \frac{1}{\varepsilon}\rho(\mathbf{u} \bullet \nabla)\mathbf{u}\frac{1}{\varepsilon} = -\nabla p + \mu\frac{1}{\varepsilon}\nabla^{2}\mathbf{u} - \frac{\mu}{\kappa}\mathbf{u}$$
(3.5)

where ε is the porosity of the porous domain and κ is the permeability of the domain in m^2 .

Permeability, κ , is calculated using the Kozeny-Carmen equation:

$$\kappa = \frac{\varepsilon^3}{c_\kappa \tau^2 a_\nu^2} \tag{3.6}$$

where c_x is the Kozeny constant, τ is tortuosity of the porous media and a_y is the surface area of the porous electrode.

Conservation of mass of each species gives:

$$\frac{\partial \varepsilon c_i}{\partial t} + \nabla \bullet N_i = S_i \tag{3.7}$$

where the flux of species i (H⁺, Pb²⁺, CH₃SO₃⁻) in mol m⁻² s⁻¹, N_i is calculated using the Nernst-Planck equation.

$$N_i = -D_{i,eff} \nabla c_i - z_i u_{m,i,eff} F c_i \nabla \phi + u c_i$$
(3.8)

For species i, S_i is its source term, described in Table 1, $D_{i, eff}$ is its effective diffusion coefficient in m^2 s⁻¹, c_i is its concentration in mol m^{-3} , z_i is its valence and $u_{m, i, eff}$ is its effective mobility in s mol kg⁻¹. ϕ is the electrolyte potential in V, F is Faraday's constant in C mol⁻¹.

The mobility, $u_{m,\ i}$ was such that the conductivity closely matches experimental measurements by Krishna et al. [30]. The method for calculating this is explained in a previous study [32].

 Table 2

 Initial conditions applied to the simulations of SLFBs.

Variable	Initial value	Unit	
и	0	${\rm m}~{\rm s}^{-1}$	
ν	0	${ m m~s^{-1}}$	
p	0	Pa	
$cPbII_0$	700	$ m mol~m^{-3}$	
cH_0	1000	$ m mol~m^{-3}$	
ϕ_l	0	V	
ϕ_s	0	V	
$\phi_{s,+}$	0	V	
$a_{\nu,10}$	620	m^{-1}	
$a_{v,30}$	1400	m^{-1}	
$a_{v,45}$	1450	m^{-1}	
$a_{v,80}$	1700	m^{-1}	
$a_{\nu,100}$	1450	m^{-1}	
ε	0.97	-	
μ_{e0}	1.6762	mPa s	
$ ho_{e0}$	1.727	${\rm kg~dm^{-3}}$	

In the porous electrode:

$$D_{i,eff} = F_d D_i \tag{3.9}$$

$$\sigma_{s.eff} = (1 - \varepsilon)F_s\sigma_s \tag{3.10}$$

where F_d is the correction factor for diffusion and F_s is the correction factor for electrical conductivity. In the Bruggeman case, $F_d = \varepsilon^{1.5}$ and $F_s = (1 - \varepsilon)^{1.5}$. $D_{i, eff}$ is the effective diffusion coefficient of species i in m^2 s⁻¹, ε is the electrode porosity and D_i is the diffusion coefficient of species i in m^2 s⁻¹. $\sigma_{s, eff}$ is the effective conductivity of the electrode and σ_s is the conductivity of the electrode both in S m^{-1} .

The current in the solid phase of the porous electrode is determined by Ohm's law:

$$i_s = \sigma_{s,eff} \nabla \phi_s \tag{3.11}$$

In the free electrolyte, $D_{i, eff} = D_{i}$ and therefore, $u_{m, i, eff} = u_{m, i}$.

3.2. Boundary conditions

A fully developed laminar inflow condition was prescribed by virtually extruding the inlet by length L_{in} and applying a pressure to the end of the virtual domain such that when solving Eq. (3.5) there was a desired average velocity at the inlet, see Eq. (3.12). The no-slip boundary condition was applied at the current collector surface.

$$-p_{in}\mathbf{n} = L_{in}\left(-\nabla p + \mu \frac{1}{\varepsilon}\nabla^2 \mathbf{u}\right) \tag{3.12}$$

where p_{in} is the inlet pressure, n is the normal vector, L_{in} is the inlet length, p is the local pressure, μ is viscosity, ε is the porosity, and u is velocity,.

$$u = 0, \quad v = 0$$
 (3.13)

At the outlet, pressure and diffusive fluxes and current density normal to the outlet boundary are equal to zero.

$$-D_i \nabla c_i \bullet \mathbf{n} = 0, \qquad \mathbf{j} \bullet \mathbf{n} = 0, \qquad p = 0 \tag{3.14}$$

Inlet concentrations for each species were calculated assuming perfect mixing in the reservoir, Eq. (3.15).

$$c_{in,i} = \int \frac{L}{V} \left(\int_{outlet} N_i \bullet \mathbf{n} \ dS - \int_{inlet} N_i \bullet \mathbf{n} \ dS \right) dt \tag{3.15}$$

where L is the width of the cell out of plane and V is the electrolyte reservoir volume.

The porosity of each electrode varied with volume of deposited material, i.e. state of charge. The change in porosity was calculated using Faraday's law, Eq. (3.16). 100% efficiency of the deposition

reactions in the electrodes was assumed, and the deposits were considered to form as fully dense materials on the RVC surface with densities for Pb and PbO₂ as described in Table 3.where for solid species, j, c_j is its concentration, ρ_j its density, M_j its molar mass and S_j its source term, described in Table 1.

As is typical in SLFB models, [14–18,28,32], Butler-Volmer kinetics were used, described by Eqs. (3.18) and (3.19) for the negative and positive reactions, respectively. The positive side reaction uses a modified Butler-Volmer equation, as seen in previous SLFB models, [14,28], to describe the kinetics, Eq. (3.20). To account for the availability of solid species in the reaction kinetics during discharge, when the solid surface concentration approached 0, the surface area in the porous domain tended to 0 during discharge. This represents the active surface area, as the discharge (dissolution) reaction only occurs at the surface of the deposits, not at the stripped RVC surface. A smoothed Heaviside function, using a piecewise 5th degree polynomial equation was used to transition between the two equations, between 0 and 1 mol m $^{-3}$. As the terms c_{PbO2} and c_{PbO} are included in Eq. (3.20), discontinuity is not required.

Negative electrode:

$$i_{loc} = Fk_{0,Pb}c_{Pb^{2+}}\left(e^{\left(\frac{a_{o,neg}F\eta_{neg}}{RT}\right)} - e^{\left(\frac{-a_{r,neg}F\eta_{neg}}{RT}\right)}\right)$$

$$i_{v} = \begin{cases} a_{v,neg}i_{loc} & c_{Pb} > 0\\ 0 & c_{Pb} = 0 \text{ during discharge} \end{cases}$$
(3.18)

Positive electrode:

Main reaction

$$i_{loc} = Fk_{0,PbO_{2}}c_{Pb^{2+}}\frac{c_{H^{+}}}{c_{H^{+}_{ref}}}\left(e^{\left(\frac{a_{0,pos}F\eta_{pos}}{RT}\right)} - e^{\left(\frac{-a_{r,pos}F\eta_{pos}}{RT}\right)}\right)$$

$$i_{v} = \begin{cases} a_{v,pos}i_{loc} & c_{PbO_{2}} > 0\\ 0 & c_{PbO_{2}} = 0 \text{ during discharge} \end{cases}$$
(3.19)

Side reaction

$$i_{loc} = F\left(k_{f,PbO}c_{PbO}^{2}e^{\left(\frac{F\eta_{Dos}}{RT}\right)} - c_{H^{+}}c_{PbO_{2}}k_{b,PbO}e^{\left(\frac{F\eta_{Dos}}{RT}\right)}\right)$$

$$i_{v} = a_{v,pos}i_{loc}$$
(3.20)

where i_{loc} is the local current density in A m⁻², i_V is the local volumetric current density in A m⁻³, a_V is the surface area per unit volume in m⁻¹, k_0 , p_b and k_0 , p_{bO2} are rate constants and k_{f_1} , p_{bO} is the forward rate constant for the side reaction, and k_b , p_{bO} is the backward rate constant for the side reaction in m s⁻¹, α is the transfer coefficient. Subscripts o and r represent the anodic (oxidation) and cathodic (reduction) reactions, and pos and neg denote positive and negative electrodes. η is the overpotential in V and is defined by Eq. (3.21).

$$\eta = \phi_s - \phi_l - E_{eq} \tag{3.21}$$

 ϕ_s is the electrode potential and ϕ_l is the electrolyte potential in V, and E_{eq} is the equilibrium potential in V, calculated at each electrode using the Nernst equation, Eqs. (3.22a) and (3.22b).

Negative
$$E_{Eq} = E_0 + \frac{RT}{zF} ln \left(\frac{c_{Pb}}{c_{ref}}\right)$$
 (3.22a)

Positive
$$E_{Eq} = E_0 - \frac{RT}{zF} ln \left(\frac{c_{Pb}}{c_{U+}}\right)$$
 (3.22b)

Table 3Parameters used in the solution of the simulated SLFBs.

Parameter	Value	Unit	Reference
A	0.51	$dm^{3/2} mol^{-1/2}$	[32]
В	3.29	$dm^{3/2} mol^{-1/2}$	[32]
b_1	3.52243	$ m dm^3~mol^{-1}$	[32]
b_2	0.94331	$ m dm^3~mol^{-1}$	[32]
b_3	0.18444	$ m dm^3~mol^{-1}$	[32]
D_{PbII}	7e-10	${ m m}^2 { m s}^{-1}$	[28]
D_H	9.3e-9	${ m m}^2 { m s}^{-1}$	[28]
D_{CH3SO3}	1.33e-9	${ m m}^2 { m s}^{-1}$	[32]
k_{Pb}^0	2.1e-7	${ m m~s^{-1}}$	[28]
k_{PbO2}^0	2.5e-7	${ m m}~{ m s}^{-1}$	[28]
k_b^0	4.5e-7	$mol \ m^{-2} \ s^{-1}$	[28]
k_f^0	0.002	$mol \ m^{-2} \ s^{-1}$	[28]
K	11.25	_	
ρ_{Pb}	11.337	kg dm ⁻³	[33]
ρ_{PbO2}	9.65	kg dm ⁻³	[33]
ρ_{PbO}	9.53	kg dm ⁻³	[33]
σ_{Pb}	4.69e6	${ m S~m^{-1}}$	[34]
σ_{PbO2}	8000 ^a	${ m S~m^{-1}}$	[35]
σ_{RVC}	330	${ m S~m}^{-1}$	[36]
T	300	K	
z_{PbII}	2	_	
z_{H+}	1	_	
ZCH3SO3-	-1	_	

^a Approximated constant value based on a mixture of α - and β -phases.

where E_0 is the reduction potential in V at the reference concentration, $c_{ref}R$ is the universal gas constant in J K⁻¹ mol⁻¹, T is the temperature in K.

The negative current collector is grounded:

$$\phi_s = 0 \tag{3.23}$$

At the positive current collector surface, an average current density is applied such that:

$$-\frac{\int_{\partial \mathcal{Q}} i \bullet n \ dS_{+}}{S_{+}} = i_{average}$$
 (3.24)

3.3. Initial conditions

Initial values for parameters used in the simulations are displayed in

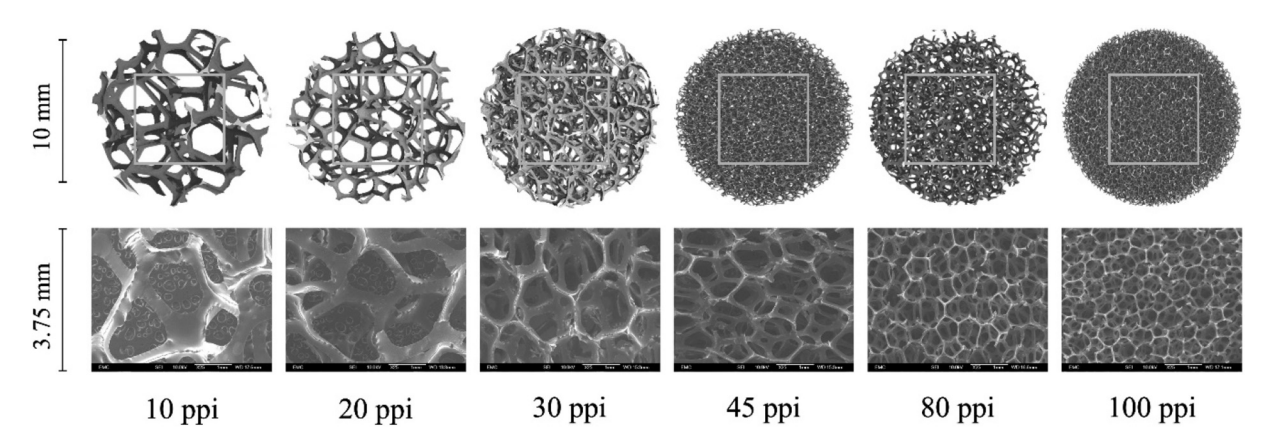


Fig. 2. Thresholded top views and greyscale views of the RVC CT data for 10 ppi, 20 ppi, 30 ppi, 45 ppi, 80 ppi and 100 ppi. The datasets are cropped to the pink (lighter coloured) box of dimensions $1072 \times 1104 \times 1296$. (For interpretation of the references to colour in this figure legend, the reader is referred to the web version of this article.)

$$\Delta \epsilon = \sum_{i} \frac{c_{j}}{\rho_{i} M_{i}} \tag{3.16}$$

$$\frac{\partial c_j}{\partial t} = S_j \tag{3.17}$$

Table 2. Initial concentrations similar to those in the literature were chosen with corresponding values for density and viscosity [10]. The remaining initial values were selected to ensure consistency with the boundary conditions. To ensure non-conflicting boundary and initial conditions, several initial values were set to 0. The boundary conditions were then applied with a smoothed Heaviside function, which uses a piecewise 5th degree polynomial equation, applied over the first 1.5 s of the simulation.

3.4. Parameters

Values of parameters used in the simulations are displayed in Table 3. The majority are as defined in our previous publications [28,32].

3.5. Numerical details

The equations were implemented and solved using COMSOL Multiphysics version 5.4. A Multifrontal Massively Parallel Sparse (MUMPS) direct solver was used for all simulations, and an implicit Backward Differentiation Formula (BDF) method was employed to control the time steps taken. First-order discretisation was employed for velocity and pressure, while linear discretisation was employed for concentration and potential fields. When compared with quadratic discretisation for concentrations and potential, a negligible difference was found.

Each domain was meshed using rectangular elements with 30 elements across the width of each electrode domain and 200 elements across the height of all domains. The elements were distributed symmetrically, with elements decreasing in size arithmetically such that the central elements were 30 times the size of the outer elements. A similar distribution was employed across the width of the electrode domains such that the inner elements were five times larger than the outer elements. Further boundary layer elements were used at the outer boundaries of the entire domain. The total number of elements ranged from approximately 13,000 to 19,000 depending on the problem solved.

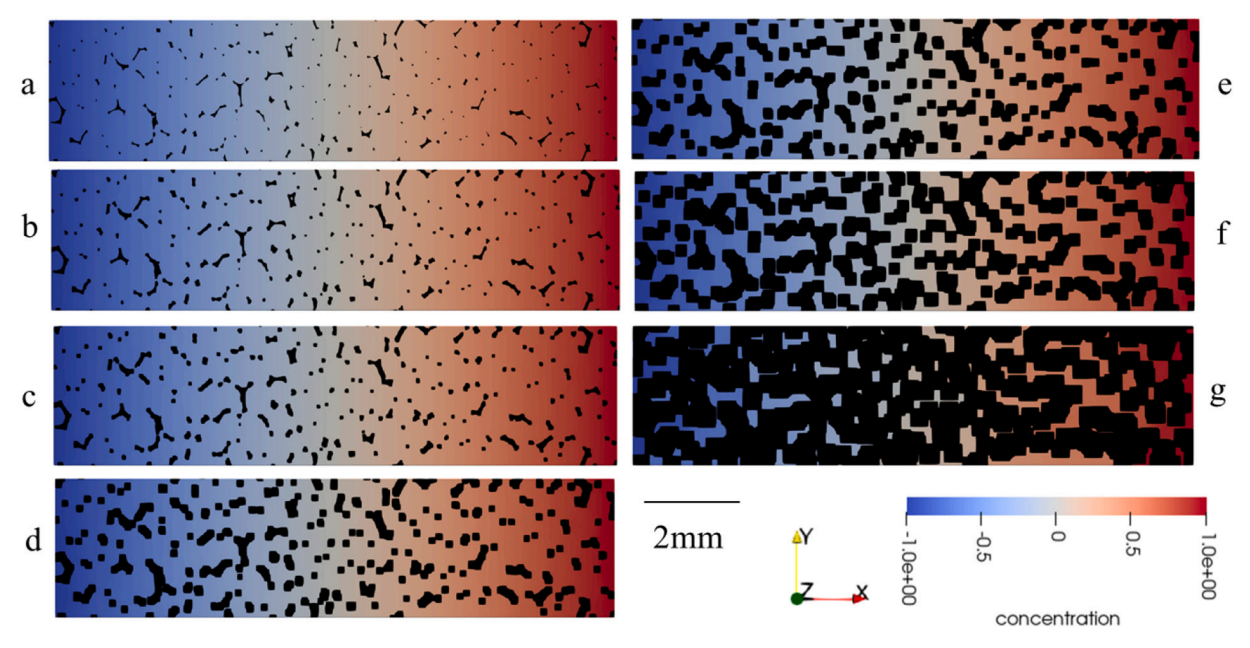


Fig. 3. Steady-state diffusion profiles for the 100 ppi RVC sample at each deposition: (a) clean, (b) one voxel dilation, (c) 10% solid volume fraction, (d) 20% solid volume fraction, (e) 30% solid volume fraction, (f) 50% solid volume fraction and (g) 80% solid volume fraction. Flow is from left to right and these are 2D representative strips of the full datasets.

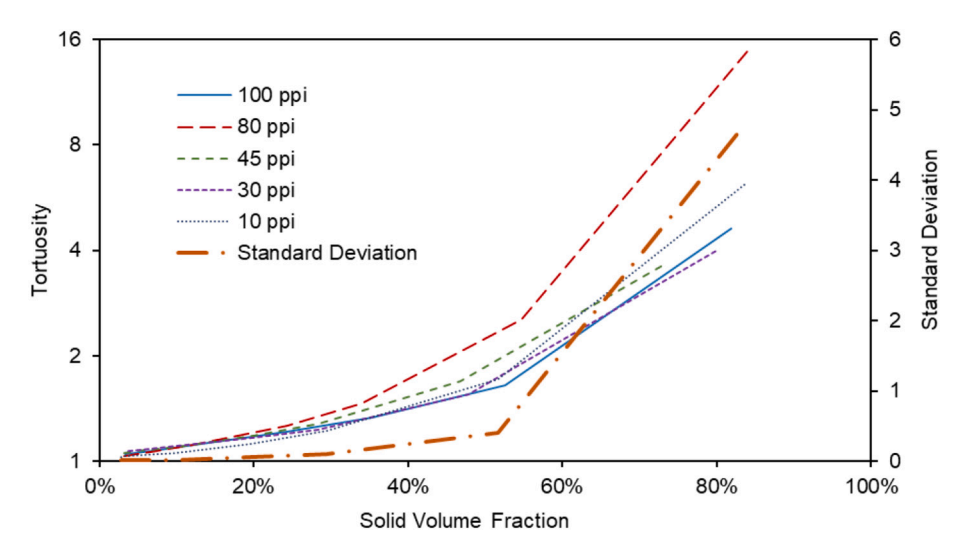


Fig. 4. Graph to show how the tortuosity of the RVC samples varies depending on the solid volume fraction and ppi value. The standard deviation between results significantly increases at higher lead deposition (i.e. 80% solid volume fraction).

4. Image data (CT)

4.1. Computational setup

Reticulated vitreous carbon electrode substrates were physically imaged to provide the scaffold geometries for the model. The raw CT data was obtained from work by Arenas et al., which used a Nikon/X-Tek XTH 225 instrument, with an isotropic resolution of 9.6 μm per voxel and a detector size of 2000 \times 2000 pixels [36]. The data for scans of 10, 30, 45, 80 and 100 ppi (pores per inch) was binarised into two constituent phases, solid and porous volume, and cropped into a cuboid domain of dimensions $1072\times1104\times1296$. Thresholded and greyscale views of 10 ppi, 20 ppi, 30 ppi, 45 ppi, 80 ppi and 100 ppi data is shown in Fig. 2.

For each grade of RVC, the morphology of the porous electrodes was virtually modified [37] by voxel dilation of the solid domain of the RVC

CT dataset in the open-source software ImageJ [38]. This virtual dilation was performed to see the effect of deposit accumulation on the transport processes of the porous electrode. The dilated volume corresponded to the volume of electrodeposited material, which is assumed to grow uniformly at all points of the porous substrate. Each dataset was dilated by a single voxel and then further dilated until the following specified total solid volume fractions were reached: 10%, 20%, 30%, 50% and 80%. Both the original and newly dilated 8-bit datasets had the raw greyscale values multiplied by 0.5 to achieve an electrolyte phase of 0 and a solid phase of 127. The original dataset was then added to each of the dilated datasets to achieve a three-phase segmented dataset with RVC holding a value of 255, the artificial electrode deposit 127 and the electrolyte 0.

The porosity and tortuosity values for each of these 35 datasets were calculated using the open-source software, OpenImpala [39]. These calculations were performed only in the *x*-direction, as work by Arenas

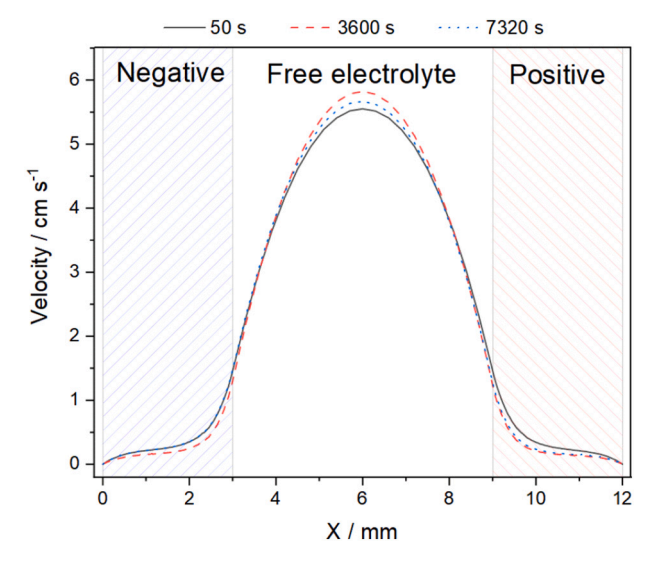


Fig. 5. Velocity profile across the mid-height of the electrodes of the undivided cell using 10 ppi RVC and an applied current density of 20 mA cm $^{-2}$. While a roughly parabolic flow profile is seen within the electrolyte domain, a sharp decrease in velocity is seen within the porous electrodes. Peak flow velocity in the electrolyte domain changes by approximately 0.2 cm s $^{-1}$ between charge and discharge. A much greater change in velocity is seen in the negative electrode between charge and discharge, where the velocity is generally greater overall. The negative (left, blue) and positive (right, red) electrodes domains are highlighted. (For interpretation of the references to colour in this figure legend, the reader is referred to the web version of this article.)

et al. showed each RVC grade had good isotropy [36]. Tortuosity, in this case, refers to effective tortuosity, not geodesic tortuosity [40], and is calculated by solving a steady-state Fickian diffusion problem:

$$D^{eff} = D \frac{\varepsilon}{\tau} \tag{4.1}$$

where τ is the tortuosity, ε the volume fraction, D^{eff} the effective diffusivity of the conducting phase and D the intrinsic diffusivity [39]. The computations were performed on the University of Southampton's supercomputer, Iridis 5 [41].

The surface area for each dataset was calculated using the surface area analysis function in the ImageJ plugin BoneJ [42]. This approximates the surface area of the dataset by creating a surface mesh from the raster dataset and then calculates the surface area of the mesh.

5. Results and discussion

5.1. Virtual dilation

Fig. 3 shows the steady-state diffusion gradients for each of the seven datasets of the 100 ppi RVC sample. Visual inspection shows that at higher levels of lead compound deposition, pathways throughout the domain have been closed off, leading to more contorted diffusion paths. Additionally, the closing of transport paths could lead to areas of the solid fraction being inaccessible on discharge, reducing ion transport. Therefore, managing lead compound accumulation in the porous electrode is a key component in the correct operation of the soluble lead flow battery.

Fig. 4 shows the complete plot of results from the image analysis. Effective tortuosity values are plotted against solid volume fraction for each of the RVC grades. There is a general trend of tortuosity increasing as lead is accumulated on the electrode, with a significant increase

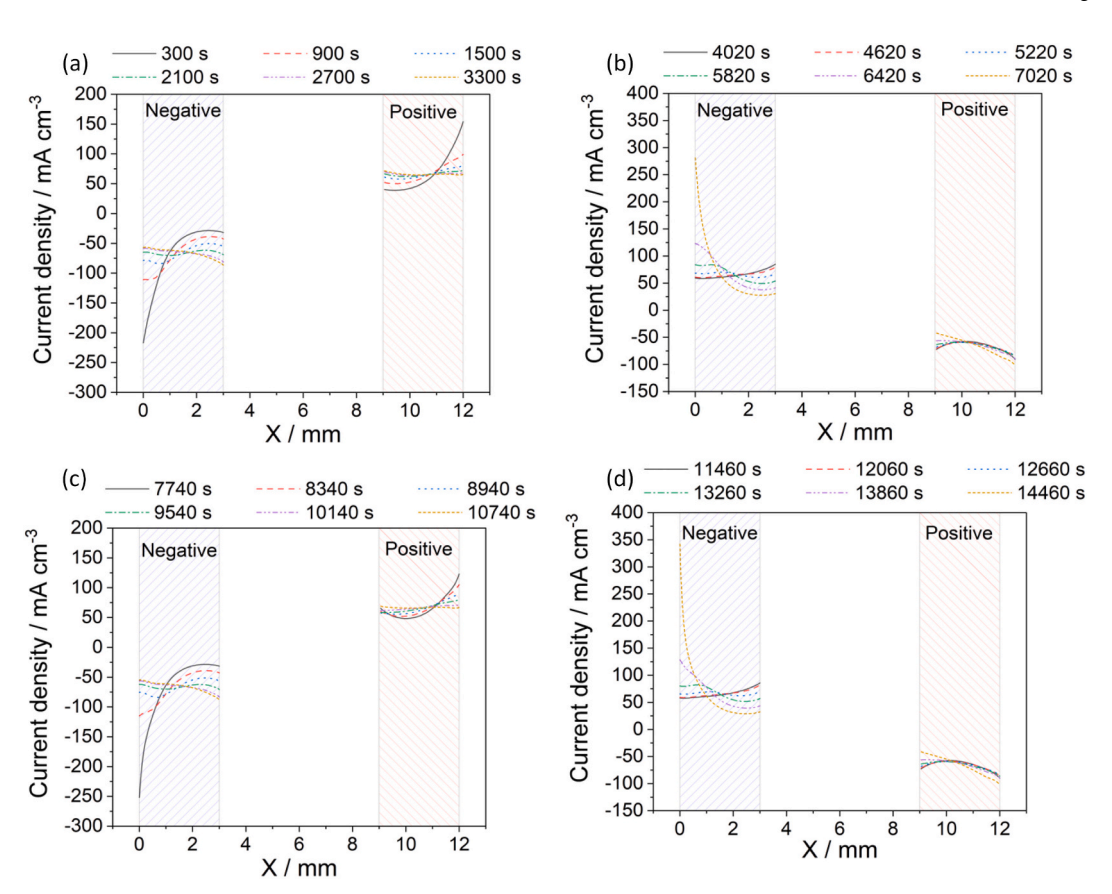


Fig. 6. Current distribution in the x-direction at the mid-height of the electrodes for the undivided configuration of the 10 ppi electrodes with an applied current density of 20 mA cm⁻² for the first charge (a), the first discharge (b), the second charge (c) and the second discharge (d).

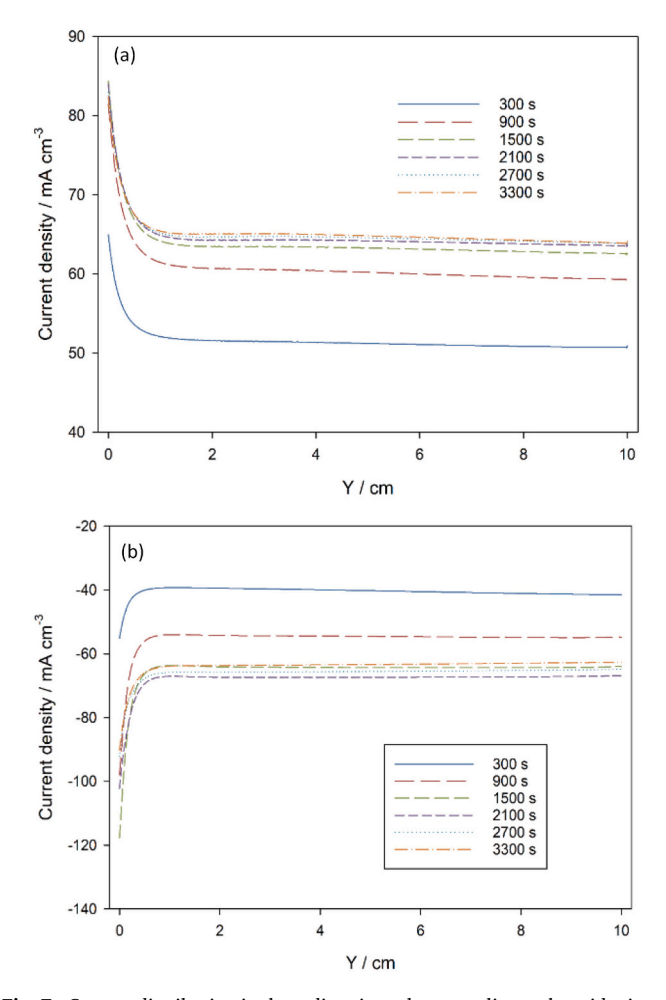


Fig. 7. Current distribution in the y-direction taken as a slice at the midpoint of the electrode domains for the 10 ppi electrodes. y=0 is at the inlet at the bottom of the cell. The distribution is shown in the positive electrode (a) and the negative electrode (b). There is a significantly increased current density in both electrodes in the first 1 cm of the domain. Current density varies with time as the current is not even in the x-direction.

apparent at values of 80% solid, likely due to the closing of transport paths. Additionally, standard deviation across the grades increases with tortuosity. At low levels of deposition, the value of tortuosity is found to be similar across the grades of RVC, which is in agreement with Arenas et al. [36]. However, as the solid fraction increases, discrepancies between the different grades become more significant. This is a key result. At low levels of deposition, the morphology of the RVC electrode appears to have little effect on transport processes, but as lead compounds are accumulated, the structure becomes increasingly important.

Furthermore, the 80 ppi grade has a significantly higher tortuosity value, ~ 15.2 , at a solid volume fraction of 80%. The specific morphology of this grade has resulted in a very contorted diffusion path. When designing electrodes for use in the soluble lead flow battery, it is important to consider the effect of morphology on both the transport processes occurring in a fully discharged state and in a fully charged state when lead compound accumulation is higher.

The tortuosity and porosity values obtained through these methods are then used as values in a lookup table for the numerical model to represent the varying conditions throughout charge/discharge accurately. At each timestep, the volume fraction is taken, and a linear interpolation function is used with the lookup table to determine the corresponding values of tortuosity and porosity.

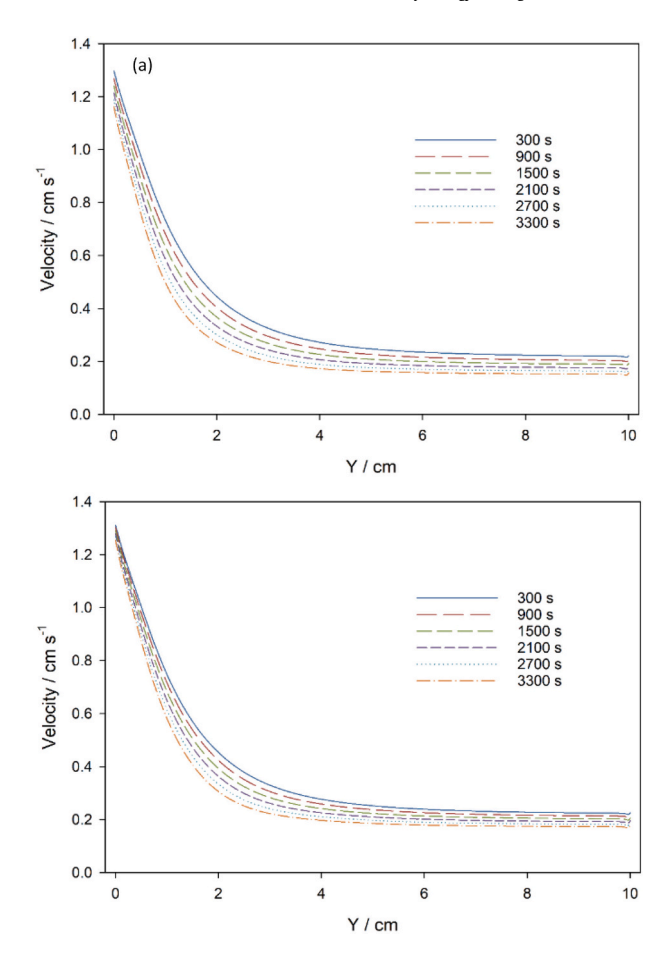


Fig. 8. Velocity distribution in the y-direction at the midpoint of the 10 ppi positive electrode (a) and negative electrode (b). The velocity begins at over 1 cm s $^{-1}$ near the inlet in both electrodes but rapidly reduces with increased distance from the inlet. The change in velocity levels off after approximately 4 cm and remains relatively constant between 1.5 and 3 mm s $^{-1}$ in both electrodes.

5.2. Undivided cell

Initially, the cell was set up with 3 mm RVC domains at the positive and negative electrodes, separated by a 6 mm electrolyte domain. See Fig. 1(a). The total gap between current collectors was 12 mm. For each grade of RVC described, an applied current density of 20, 30 and 50 mA cm $^{-2}$ was applied at the positive current collector boundary for a duration of 1 h. The cell was then discharged with the same applied current density until the cell voltage dropped to 1.3 V.

A value of 1.3 V was chosen as the discharge cut-off voltage because, after this point, the cell potential drops sharply [9]. While a lower cut-off voltage does not change the discharge time significantly, it added a significant amount of computational time due to the very short time-stepping required to calculate the period of rapid potential change. For brevity, general trends from the simulation results are discussed using the 10 ppi case as a representative example. Other grades of RVC are included where relevant comparisons are made.

Fig. 5 shows the velocity profile across the cell, where 0–3 mm corresponds to the negative electrode domain, 3–9 mm to the electrolyte domain and 8–12 mm to the positive electrode domain. The velocity profile is shown just after the start of the first charge ($t = 50 \, s$), at the end of the first charge period ($t = 3600 \, s$) and at the end of the first discharge period ($t = 7320 \, s$).

In this configuration, as seen in Fig. 5, the electrolyte velocity is considerably lower in the porous electrodes than in the free electrolyte, even at initial conditions and for the RVC grade with the largest pore size

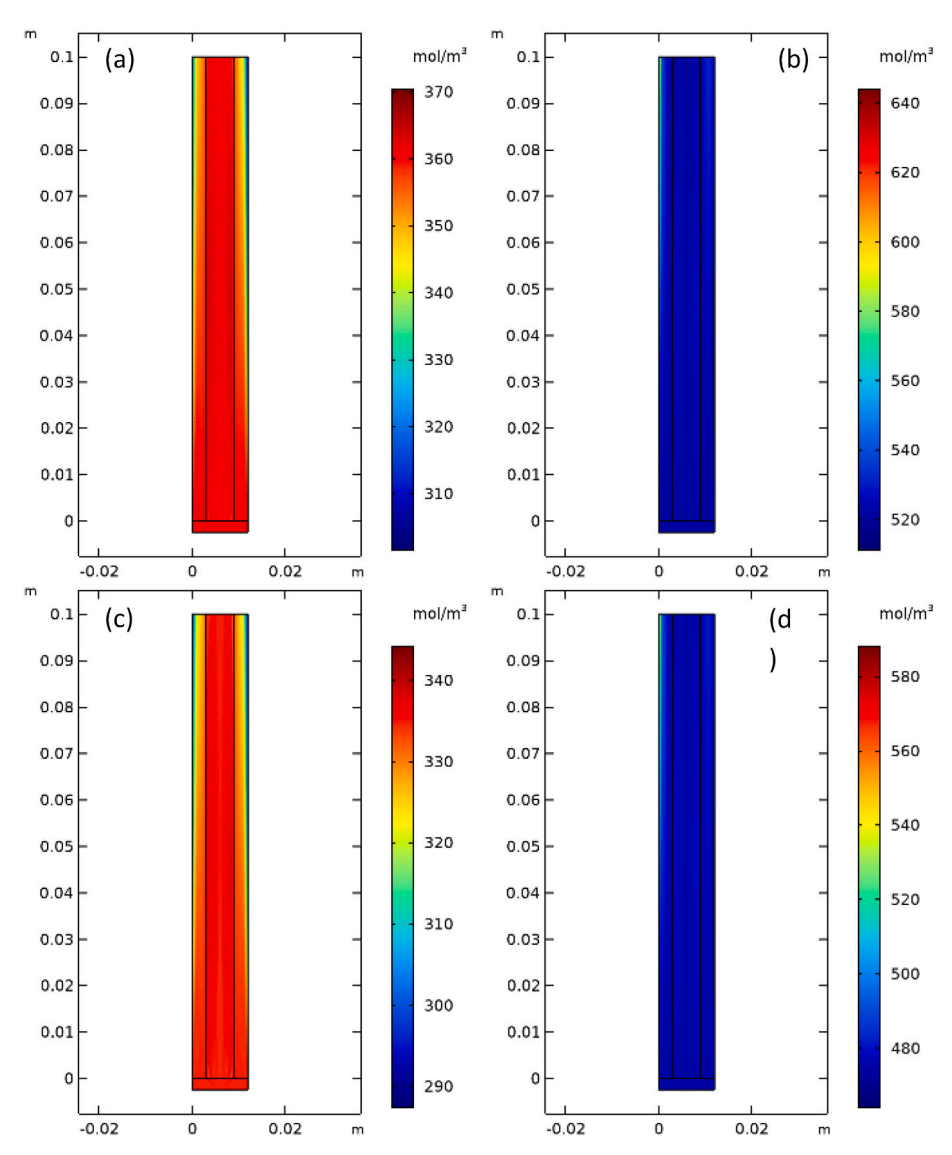


Fig. 9. Pb²⁺ concentration distribution near the end of the first charge for the 50 mA cm⁻² cell using 10 ppi electrodes during charge 1 (a), discharge 1 (b), charge 2 (c) and discharge 2 (d).

(10 ppi). It can be seen that after the first charge, when the velocity distribution changes by a similar magnitude, the velocity in the positive electrode stays very low during the remaining cycles, irrespective of SoC. However, the velocity in the negative electrode returns to near its initial value at the end of discharge. This is due to the side reaction at the positive electrode meaning solid PbO remains even after discharge. Therefore, the positive electrode permeability remains lower than that of the negative electrode. The peak velocity in the middle of the electrolyte domain increases as deposits are built up within the electrodes. More electrolyte is forced through the lower resistance, free electrolyte domain.

The current density in the porous electrodes varied spatially in both x and y directions. Fig. 6 shows the current distribution in the x-direction at regular intervals during each charge and discharge. The first charge is from 0 to 3600 s, the first discharge from 3720 to 7320 s, the second charge from 7440 to 10,740 s and the second discharge from 11,160–14,760 s. For each grade of RVC and at all applied current densities, the current was initially highest near the current collectors. As the cell charged, the current density became more evenly distributed in the x-direction.

The current density was highest near the inlet throughout charge and discharge in both electrodes. Fig. 7 shows the current distribution in the

y-direction at the midpoint of both porous electrodes. There was a substantial increase in current density in both electrodes in the closest 1 cm to the inlet.

As such, as charging continued, the higher deposition rate reduced the porosity near the inlet. The electrolyte flow was, therefore, further diverted around the electrodes. In Fig. 8, which shows the electrolyte velocity distribution in the y-direction at the midpoints of both electrodes, the electrolyte velocity distribution is shown to be uneven in the y-direction as the charge cycle continues. Throughout cycling, the electrolyte velocity decreases sharply in the first few cm of the electrodes.

By the end of the first charge, the flow in the top 6 cm of both electrodes drops below 2 mm s $^{-1}$, less than 10% of the bulk velocity. Fig. 9 shows the concentration distribution after 3550 s, shortly before the end of the first charge. Here it is seen that with the reduced electrolyte flow, the Pb $^{2+}$ concentration within the electrodes was not readily replenished. Near the outlet, the Pb $^{2+}$ concentration in both electrodes drops to below 0.1 mol dm $^{-3}$.

Fig. 10 shows the concentration distribution across the cell at the midpoint of the electrodes at varying times and current densities for each RVC grade. At higher rates of charge and grades of RVC with a larger number of pores, the concentration gradients are larger; for all

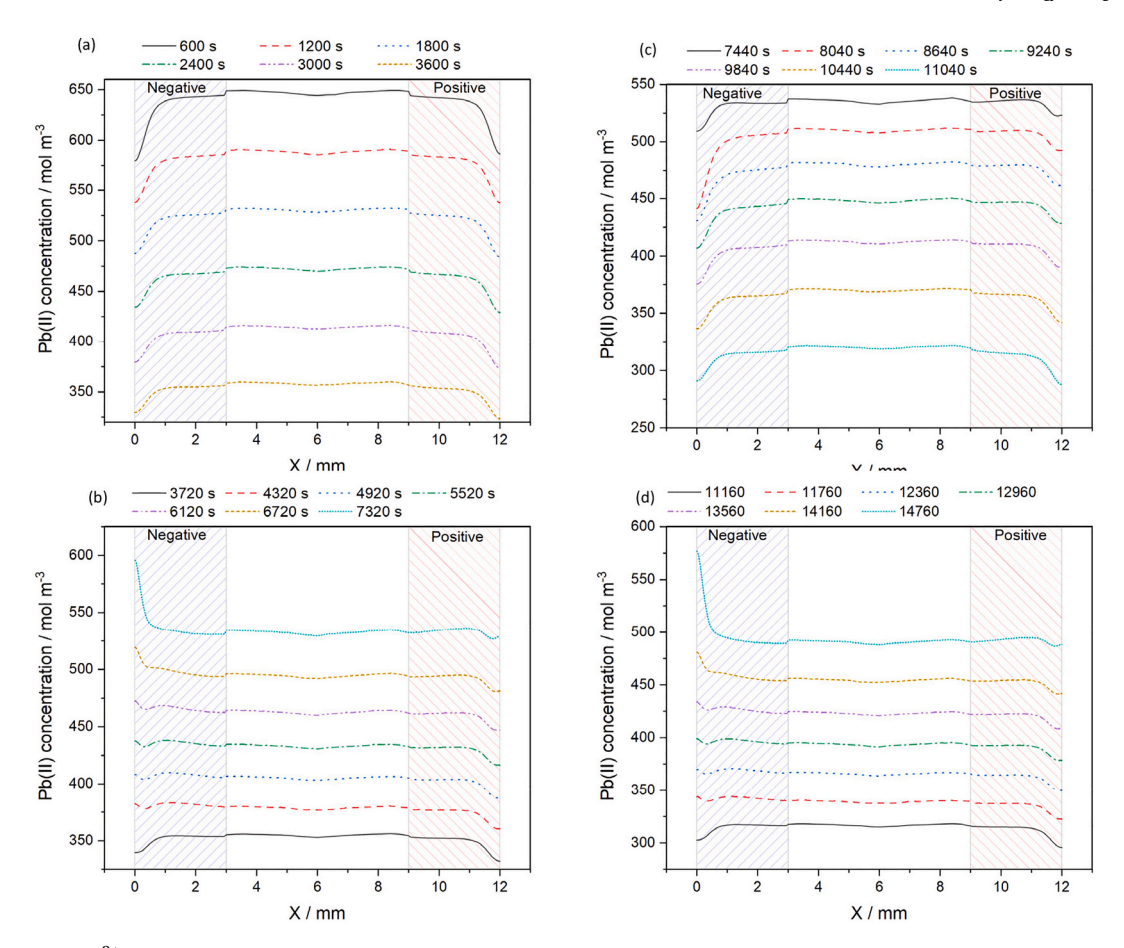


Fig. 10. Distribution of Pb^{2+} concentration in the x-direction at the mid height of the electrodes for the undivided configuration of the 10 ppi electrodes with an applied current density of 20 mA cm⁻².

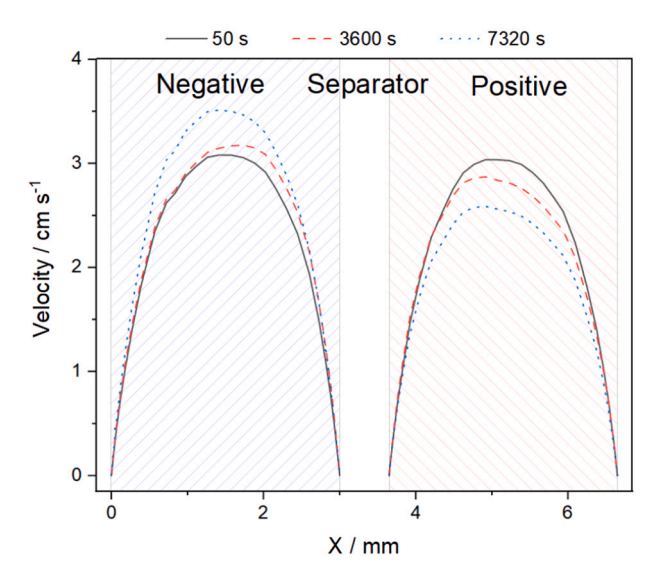


Fig. 11. Velocity profile across the mid-height of the electrodes of the divided cell using 10 ppi RVC and an applied current density of 20 mA cm $^{-2}$. A parabolic distribution remains throughout charging. As the SoC increases, the velocity in the negative electrode increases, while it decreases in the positive electrode

cells at 50 mA cm $^{-2}$ near the end of charge, the Pb $^{2+}$ concentration drops to below 0.1 mol dm $^{-3}$ compared to a bulk concentration of 0.22 mol dm $^{-3}$, see Fig. 9. This indicates that the electrolyte flow and

diffusion of Pb^{2+} are inadequate to maintain a high current within the electrodes near the current collector when lead utilisation in the bulk electrolyte is high. The reduced Pb^{2+} concentration leads to a higher overpotential required to maintain a current density, and hence in areas with a lower Pb^{2+} concentration, the current density is decreased. A higher current density is therefore seen close to the boundary with the bulk electrolyte. In physical cells, this may lead to Pb being deposited at the interface between the porous electrode domain and the electrolyte domain, as is described by Iacovangelo and Will during zinc deposition on porous carbon electrodes [43], negating the advantage of a lower local current density from a porous electrode.

5.3. Divided cell

The free electrolyte domain was removed to encourage a higher flow within the electrodes and overcome this reduction in Pb^{2+} concentration. Clearly, the electrodes cannot be touching, and in a physical cell, lead dendrites are common and can grow between the electrodes [10]. Hence, a non-conducting microporous separator domain was placed between the electrodes to prevent short-circuiting but to allow the transfer of ions. A typical example is microporous polyethene, which is commonly used in Zn-Br RFBs [44]. As the flow was forced through the electrodes, the velocity in the porous domains was much higher. During charge, as Pb is denser than PbO₂ and hence the same number of moles of Pb has a smaller effect on the porosity of the electrodes, the flow increased in velocity in the negative electrode and decreased in the positive electrode. However, the flow rate remained significantly higher in both electrodes than in the undivided configuration as shown in Fig. 11.

The same 1 h charge cycle was applied to this divided arrangement,

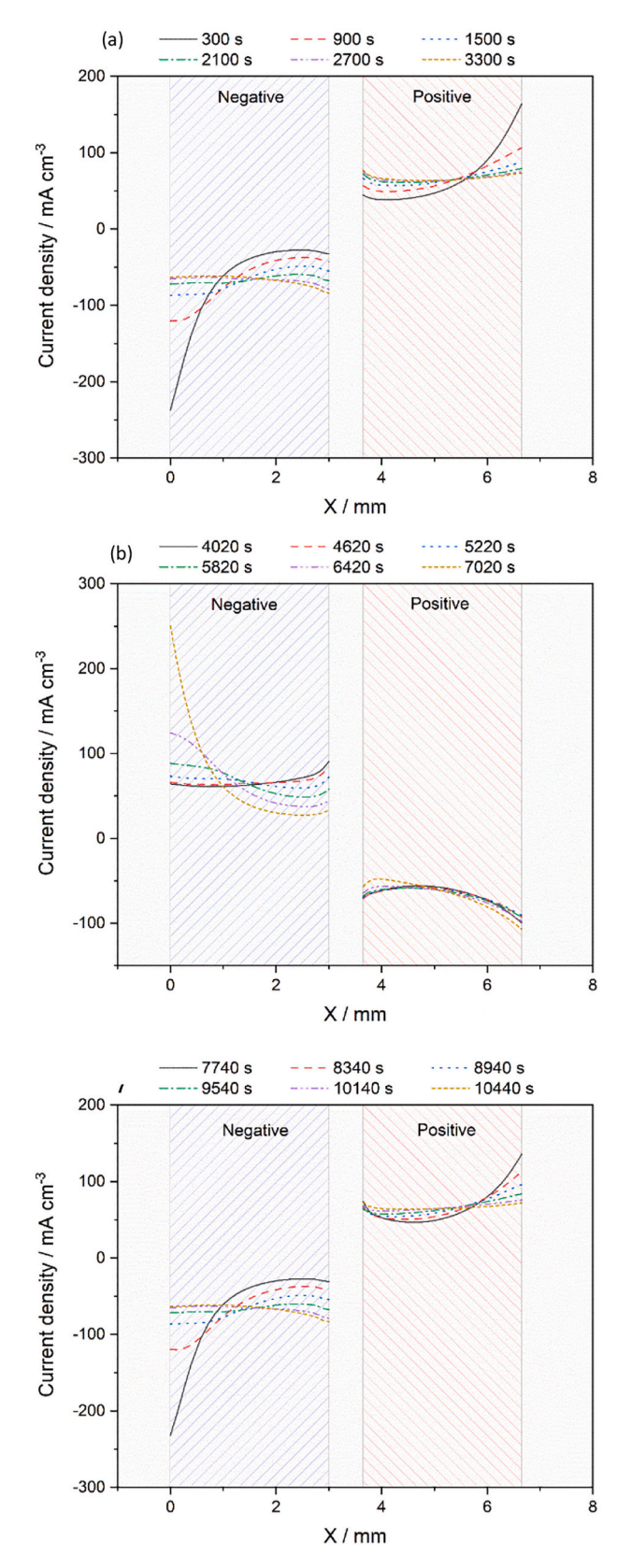


Fig. 12. Current distribution in the x-direction at the mid-height of the electrodes for the divided configuration of the 10 ppi electrodes with an applied current density of 20 mA cm $^{-2}$ during charge 1 (a), discharge 1 (b) and charge 2 (c).

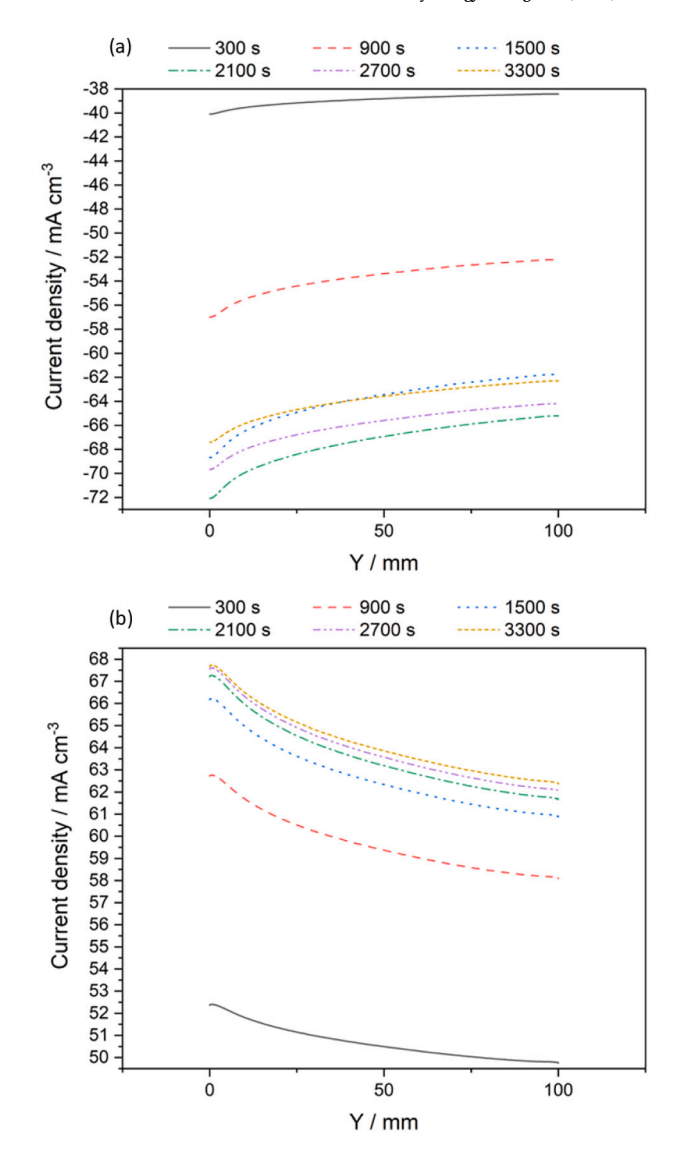


Fig. 13. Current density distribution in the y-direction at the midpoint of the 10 ppi negative (a) electrode and the positive (b) electrode of the divided cell.

with 20, 30 and 50 mA cm $^{-2}$ applied to each grade of RVC. Fig. 12 shows the current distribution in the x-direction for the divided arrangement. The distribution of current within the electrodes is very similar to that in the undivided configuration. In both configurations, there are minima seen in the current density in the x-direction. With increased distance from the current collectors, a greater proportion of current flows in the electrolyte vs the electrodes, so close to the current collectors, the electrode potential changes quickly with x and the electrolyte potential changes slowly. This trend is reversed as current moves to the electrolyte. Hence the difference in electrolyte and electrode potential initially decreases then increases again with distance from the current collectors. As seen in Eq. (3.21), this causes minima in overpotential and hence the minima seen in the current distribution.

The current density is highest closest to the current collector at the start of charge. By the end of the 1 hour charge, while there is a slight increase in current at the outer edge of both electrodes, the current distribution is far more even. The current density near the inlet is also substantially less pronounced. The current density averaged across the inlet is approximately 71 mA cm $^{-3}$ at the positive electrode and 69 mA cm $^{-3}$ in the negative electrode, compared to the average in the electrode of 67 mA cm $^{-3}$. Fig. 13 shows that while there is some variation in current density in the *y*-direction, which is expected due to the increased

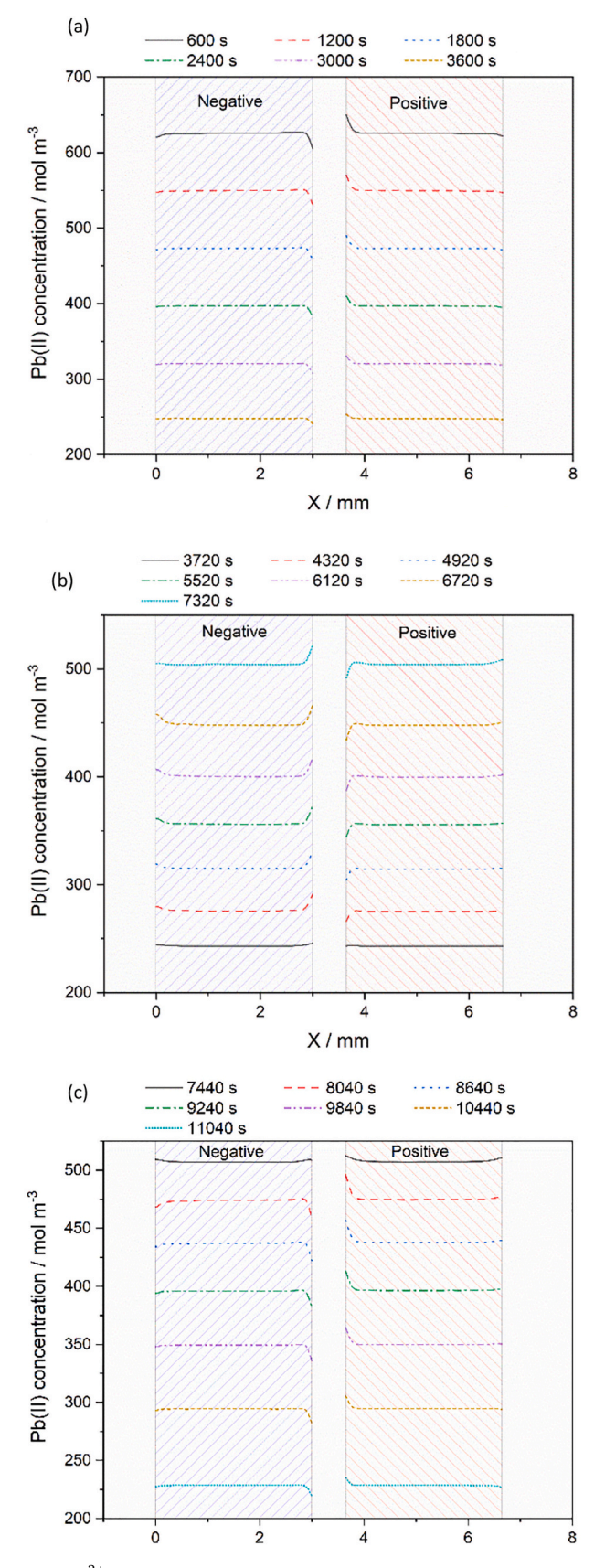


Fig. 14. Pb $^{2+}$ concentration distribution in the x-direction at the mid height of the electrodes for the divided configuration of the 10 ppi electrodes with an applied current density of 20 mA cm $^{-2}$ during charge 1 (a), discharge 1 (b) and charge 2 (c).

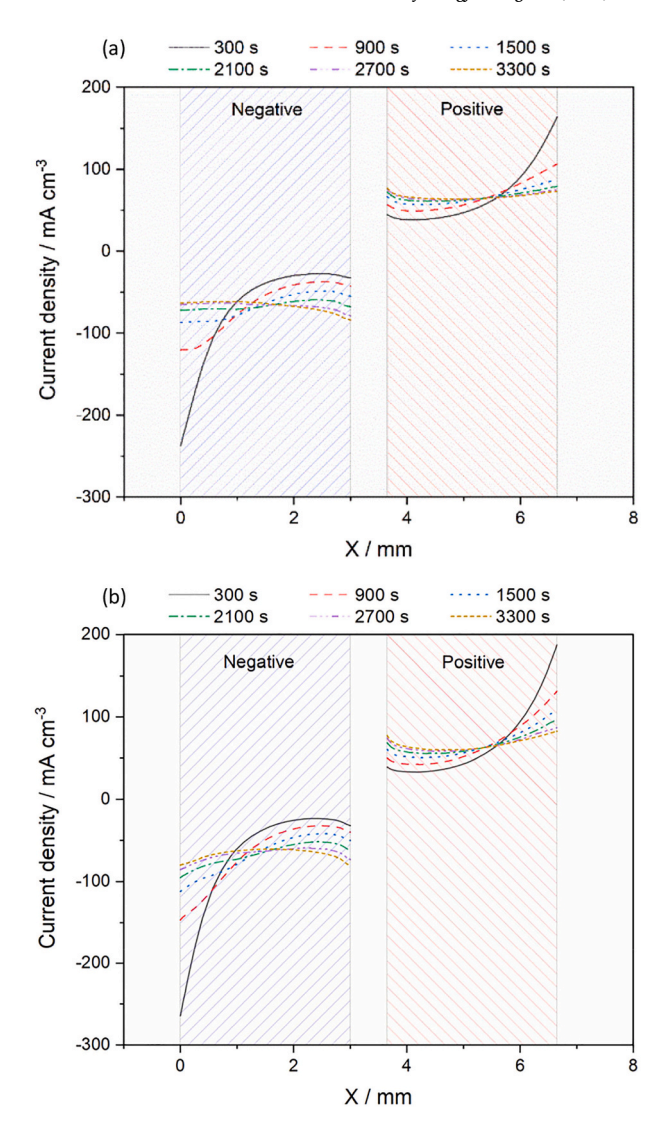
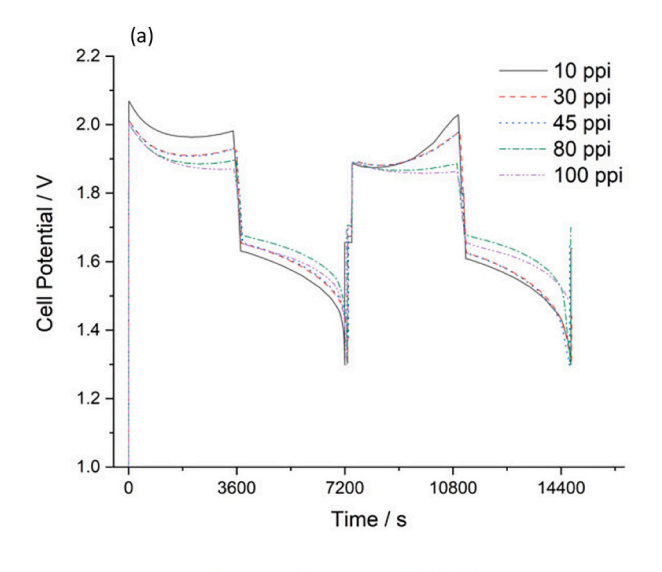


Fig. 15. Current distribution in the x-direction at the mid height of the electrodes for the divided configuration of the 10 ppi (a) and 100 ppi (b) grades of RVC with an applied current density of 20 mA cm $^{-2}$.

concentration overpotential with increased distance from the inlet, there is not the sharp increase near the inlet seen with the undivided configuration.

As the electrolyte is forced through the electrodes, the concentration of soluble species remains far more constant. There is also a virtually flat concentration profile in the x-direction other than close to the separator boundary. These effects complement work by Masliy et al., who describe the expected current density distribution for a generalised redox reaction in porous electrodes [45]. In the negative electrode, both Pb²⁺ and H⁺ concentration decrease as the separator boundary is approached during charge, while in the positive electrode, the concentration of both species increases. The opposite is true during discharge (Fig. 14).

Comparing different grades of RVC, there is little difference in the current distribution of the divided cells. However, in general, coarser grades of RVC gave a more even current distribution in the x-direction. As the cell is charged, the current distribution initially changes rapidly. However, with further charging, the current distribution stabilises. At 20 mA cm $^{-2}$, this occurs after approximately 2700 s, at 30 mA cm $^{-2}$ by 2100 s, and at 50 mA cm $^{-2}$ by 1500 s. At 50 mA cm $^{-2}$, this stable current distribution varies from circa 0.16 A cm $^{-3}$ at the current collector to 0.13 A cm $^{-3}$ at its lowest near the centre and 0.34 A cm $^{-3}$ near the membrane in the 100 ppi negative electrode. In the 10 ppi negative



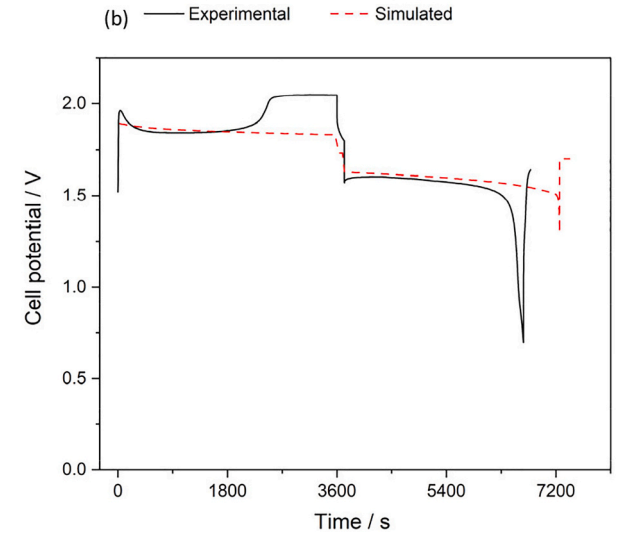


Fig. 16. Cell potential vs time for (a) different grades of RVC with an applied current density of 20 mA cm⁻³ and (b) experimental and simulated results for 80ppi RVC electrodes with an applied current density of 20 mA cm⁻², the first cycle is omitted.

electrode, it varies from $0.14 \,\mathrm{A}\,\mathrm{cm}^{-3}$ to $0.15 \,\mathrm{A}\,\mathrm{cm}^{-3}$ to $0.30 \,\mathrm{A}\,\mathrm{cm}^{-3}$, see Fig. 15. A similar trend is seen in the positive electrodes.

The most striking difference between different grades of RVC is the overpotential. This is expected, as while the starting porosity is roughly equivalent across the different grades, the surface area varies significantly. A higher surface area leads to a lower local current density, and by inspecting the Butler-Volmer equations (Eqs. (3.18)–(3.20)), it can be determined that this leads to a lower overpotential. Accordingly, the 100 ppi electrodes, which have smaller pores and hence a larger surface area, have a greatly reduced overpotential during both charge and discharge than the lower ppi electrodes. When compared to the 10 ppi electrodes, the overpotential is reduced by approximately 100 mV, see Fig. 16(a).

Fig. 16(b) shows a comparison between experimental and simulated cell potential of a cell cycled at 20 mA cm $^{-2}$ using 80 ppi RVC electrodes. The model setup was modified to match the dimensions of the experimental cell. The first cycle is omitted. The simulated potential closely matches the experimental at the start of both the charge and discharge steps. At the end of the charge, the experimental cell potential rises to approximately 2.05 V. However, the simulated voltage remains at approximately 1.85 V. This suggests that the kinetics model of the reactions at the positive electrode could be improved. As the side reaction

in this model is simplified, further work is required to fully understand and implement a more accurate model of this reaction. During discharge, while the coulombic efficiency of the experimental cell is lower, the cell potential of the simulated cell is closely matched to that of the experimental cell. In both cells, a voltage efficiency of over 80% is achieved

Applied current density appears to have a much greater impact on variation in current distribution. While the general trend of decreasing current near the current collectors and increasing near the membrane boundary is true for all the simulated applied current densities, once it has settled, the current remains approximately even throughout the electrode at 20 mA cm $^{-2}$ in the 10 ppi electrodes. However, as the current density increases, the current near the separator boundary increases more than in the remainder of the electrodes. This is true for both the positive and the negative electrodes.

One method to decrease the variability in current density within the electrodes would be to combine grades of RVC to form a graduated electrode. A similar method is used with lithium-ion batteries [46]. While it appears that there would be little benefit in this method at lower current densities, at higher currents, the region close to the separator boundary would benefit from a relative reduction in current density. This could be achieved by using a larger pore size close to the centre of the cell than for the bulk electrode. Only a small region would require this increased pore size, allowing the remainder of the electrode to take advantage of the lower overpotential and hence increased efficiency gained from using RVC with smaller pores.

6. Conclusions

A novel numerical model for investigating three-dimensional electrodes in the soluble lead flow battery, which has been validated against experimental results, has been developed. The model highlights the benefits of using reticulated vitreous carbon as an electrode material at both electrodes. The model emphasises the issues with using thin layers of RVC divided by a region of free electrolyte, as has been used in previous experimental studies of RVC in the SLFB. Even with the high permeability of RVC, there is a significant reduction in electrolyte velocity within the electrodes. A high current density is predicted near the inlet, which causes a build-up of deposit in this area, further diverting the electrolyte out of the electrode domains. Forcing the electrolyte through the RVC electrodes by replacing the free electrolyte domain with a microporous separator significantly improved the current distribution in the *y*-direction. In the divided configuration, the concentration is substantially less varied in both *x* and *y* directions.

The higher surface area of RVC with smaller pores leads to a reduction in overpotential. Comparing 100 ppi with 10 ppi RVC, there is a reduction in overpotential of over 100 mV when cycled with an applied current density of 50 mA cm $^{-2}$. At 20 mA cm $^{-2}$, a voltage efficiency of over 80% is achieved experimentally. While using a single grade of RVC for each electrode still gives an uneven current distribution, in future, by taking advantage of their different overpotentials, it may be possible to combine different grades of RVC to provide an optimal current distribution for a specific application.

Declaration of competing interest

The authors declare that they have no known competing financial interests or personal relationships that could have appeared to influence the work reported in this paper.

Acknowledgements

The authors acknowledge the use of the IRIDIS High Performance Computing Facility at the University of Southampton during the completion of this work. The authors also acknowledge the financial support received from the Engineering and Physical Sciences Research Council (EPSRC) through the Centre for Doctoral Training in Energy Storage and its Applications grant EP/L016818/1 and from UK aid from the UK Government through the Faraday Institution and the Transforming Energy Access Programme (grant number FIEE-002 – Reclaimed Electrolyte, Low Cost Flow Battery RELCo-Bat); however, the views expressed do not necessarily reflect the UK government's official policies.

References

- [1] M.S. Ziegler, J.M. Mueller, G.D. Pereira, J. Song, M. Ferrara, Y.-M. Chiang, et al., Storage requirements and costs of shaping renewable energy toward grid decarbonization, Joule 3 (9) (2019) 2134–2153.
- [2] S. Homan, N. Mac Dowell, S. Brown, Grid frequency volatility in future low inertia scenarios: challenges and mitigation options, Appl. Energy 290 (2021), 116723.
- [3] US Department of Energy, DOE Global Energy Storage Database, Available, https://www.sandia.gov/ess-ssl/global-energy-storage-database/, 2020 [Accessed:10/01/2021].
- [4] L. da Silva Lima, M. Quartier, A. Buchmayr, D. Sanjuan-Delmás, H. Laget, D. Corbisier, et al., Life cycle assessment of lithium-ion batteries and vanadium redox flow batteries-based renewable energy storage systems, Sustain. Energy Technol. Assess. 46 (2021), 101286.
- [5] S. Ha, K.G. Gallagher, Estimating the system price of redox flow batteries for grid storage, J. Power Sources 296 (2015) 122–132.
- [6] E. Sánchez-Díez, E. Ventosa, M. Guarnieri, A. Trovò, C. Flox, R. Marcilla, et al., Redox flow batteries: status and perspective towards sustainable stationary energy storage, J. Power Sources 481 (2021), 228804.
- [7] K. Orapeleng, R.G. Wills, A. Cruden, Performance of recovered and reagent grade electrolyte in a soluble lead redox cell, J.Energy Storage 20 (2018) 49–56.
- [8] K. Orapeleng, R.G. Wills, A. Cruden, Developing electrolyte for a soluble lead redox flow battery by reprocessing spent lead acid battery electrodes, Batteries 3 (2) (2017) 15.
- [9] D. Pletcher, R. Wills, A novel flow battery: a lead acid battery based on an electrolyte with soluble lead (II) part II. Flow cell studies, Phys. Chem. Chem. Phys. 6 (8) (2004) 1779–1785.
- [10] M. Krishna, E.J. Fraser, R.G.A. Wills, F.C. Walsh, Developments in soluble lead flow batteries and remaining challenges: an illustrated review, J.Energy Storage 15 (2018) 69–90, https://doi.org/10.1016/j.est.2017.10.020.
- [11] M.G. Verde, K.J. Carroll, Z. Wang, A. Sathrum, Y.S. Meng, Achieving high efficiency and cyclability in inexpensive soluble lead flow batteries, Energy Environ. Sci. 6 (5) (2013) 1573–1581, https://doi.org/10.1039/C3EE40631H.
- [12] M. Lanfranconi, H.-J. Lilienhof, All-lead-flow-batteries as promising candidates for energy storage solutions, J.Sustain.Dev.EnergyWaterEnviron.Syst. 7 (2) (2019) 343–354.
- [13] D. Pletcher, R. Wills, A novel flow battery: a lead acid battery based on an electrolyte with soluble lead(II) part III. The influence of conditions on battery performance, J. Power Sources 149 (2005) 96–102, https://doi.org/10.1016/j. ipowsour.2005.01.048.
- [14] A.A. Shah, X. Li, R.G. Wills, F.C. Walsh, A mathematical model for the soluble leadacid flow battery, J. Electrochem. Soc. 157 (5) (2010) A589–A599, https://doi. org/10.1149/1.3328520.
- [15] M.N. Nandanwar, K.S. Kumar, S. Srinivas, D. Dinesh, Pump-less, free-convection-driven redox flow batteries: modelling, simulation, and experimental demonstration for the soluble lead redox flow battery, J. Power Sources 454 (2020). 227918.
- [16] M. Nandanwar, S. Kumar, A modelling and simulation study of soluble lead redox flow battery: effect of presence of free convection on the battery characteristics, J. Power Sources 412 (2019) 536–544, https://doi.org/10.1016/j. jpowsour.2018.11.070.
- [17] M. Nandanwar, S. Kumar, Charge coup de fouet phenomenon in soluble lead redox flow battery, Chem. Eng. Sci. 154 (2016) 61–71, https://doi.org/10.1016/j. ces 2016 07 001
- [18] M.N. Nandanwar, S. Kumar, Modelling of effect of non-uniform current density on the performance of soluble lead redox flow batteries, J. Electrochem. Soc. 161 (10) (2014) A1602–A1610, https://doi.org/10.1149/2.0281410jes.
- [19] A. Bates, S. Mukerjee, S.C. Lee, D.-H. Lee, S. Park, An analytical study of a lead-acid flow battery as an energy storage system, J. Power Sources 249 (2014) 207–218, https://doi.org/10.1016/j.jpowsour.2013.10.090.
- [20] A. Oury, A. Kirchev, Y. Bultel, A numerical model for a soluble lead-acid flow battery comprising a three-dimensional honeycomb-shaped positive electrode,

- J. Power Sources 246 (2014) 703–718, https://doi.org/10.1016/j.ipowsour.2013.07.101.
- [21] L. Arenas, C.P. de León, F. Walsh, Critical review—the versatile plane parallel electrode geometry: an illustrated review, J. Electrochem. Soc. 167 (2) (2020), 023504
- [22] A. Banerjee, D. Saha, T.N.G. Row, A.K. Shukla, A soluble-lead redox flow battery with corrugated graphite sheet and reticulated vitreous carbon as positive and negative current collectors, Bull. Mater. Sci. 36 (1) (2013) 163–170, https://doi. org/10.1007/s12034-013-0426-7.
- [23] A. Czerwiński, M. Żelazowska, Electrochemical behavior of lead dioxide deposited on reticulated vitreous carbon (RVC), J. Power Sources 64 (1–2) (1997) 29–34, https://doi.org/10.1016/S0378-7753(96)02496-2.
- [24] A. Czerwiński, M. Żelazowska, Electrochemical behavior of lead deposited on reticulated vitreous carbon, J. Electroanal. Chem. 410 (1) (1996) 55–60.
- [25] R.G.A. Wills, J. Collins, D. Stratton-Campbell, C.T.J. Low, D. Pletcher, F. Walsh, Developments in the soluble lead-acid flow battery, J. Appl. Electrochem. 40 (5) (2010) 955–965, https://doi.org/10.1007/s10800-009-9815-4.
- [26] A. Hazza, D. Pletcher, R. Wills, A novel flow battery: a lead acid battery based on an electrolyte with soluble lead(II) part IV. The influence of additives, J. Power Sources 149 (2005) 103–111, https://doi.org/10.1016/j.jpowsour.2005.01.049.
- [27] F. Walsh, L. Arenas, C. Ponce de León, G. Reade, I. Whyte, B. Mellor, The continued development of reticulated vitreous carbon as a versatile electrode material: structure, properties and applications, Electrochim. Acta 215 (2016) 566–591.
- [28] E.J. Fraser, K.K.J. Ranga Dinesh, R.G.A. Wills, Development of a two-dimensional, moving mesh treatment for modelling the reaction chamber of the soluble lead flow battery as a function of state of charge for Pb and PbO2 deposition and dissolution, J.Energy Storage 31 (2020), 101484.
- [29] SGL, SIGRACELL Bipolar Plate datasheet, Available, https://www.sglcarbon.com/en/markets-solutions/material/sigracell-bipolar-plates-and-end-plates/, 2019 [Accessed:17/03/2019].
- [30] M. Krishna, L. Wallis, R. Wills, D. Hall, A. Shah, Measurement of key electrolyte properties for improved performance of the soluble lead flow battery, Int. J. Hydrog. Energy 42 (29) (2017) 18491–18498, https://doi.org/10.1016/j. ijhydene.2017.05.004.
- [31] D.A. Nield, A. Bejan, Convection in Porous Media vol. 3, Springer, 2006.
- [32] E.J. Fraser, K.R. Dinesh, R. Wills, A two dimensional numerical model of the membrane-divided soluble lead flow battery, Energy Rep. 7 (2021) 49–55.
- [33] R.H.P.D.W. Green, R.H. Perry, D.W. Green, Knovel, Perry's Chemical Engineers' Handbook, Eighth Edition, McGraw-Hill Education, 2008.
- [34] J. Cook, M. Laubitz, M. Van der Meer, Thermal conductivity, electrical resistivity, and thermoelectric power of Pb from 260 to 550 K, J. Appl. Phys. 45 (2) (1974) 510–513.
- [35] W. Mindt, Electrical properties of electrodeposited PbO2 films, J. Electrochem. Soc. 116 (8) (1969) 1076–1080, https://doi.org/10.1149/1.2412217.
- [36] L.F. Arenas, R.P. Boardman, C.P. de León, F.C. Walsh, X-ray computed micro-tomography of reticulated vitreous carbon, Carbon 135 (2018) 85–94.
- [37] J. Le Houx, D. Kramer, X-ray tomography for lithium ion battery electrode characterisation—a review, Energy Rep. 7 (2021) 9–14.
- [38] C.A. Schneider, W.S. Rasband, K.W. Eliceiri, NIH image to ImageJ: 25 years of image analysis, Nat. Methods 9 (7) (2012) 671–675.
- [39] J. Le Houx, D. Kramer, OpenImpala: OPEN source IMage based PArallisable Linear Algebra solver, SoftwareX 15 (2021), 100729.
- [40] J. Le Houx, M. Osenberg, M. Neumann, J.R. Binder, V. Schmidt, I. Manke, et al., Effect of tomography resolution on calculation of microstructural properties for lithium ion porous electrodes, ECS Trans. 97 (7) (2020) 255.
- [41] The Iridis Compute Cluster, Available, https://www.southampton.ac.uk/isolution s/staff/iridis.page [Accessed:07/07/2021].
- [42] M. Doube, M.M. Klosowski, I. Arganda-Carreras, F.P. Cordelières, R.P. Dougherty, J.S. Jackson, et al., BoneJ: free and extensible bone image analysis in ImageJ, Bone 47 (6) (2010) 1076–1079.
- [43] C.D. Iacovangelo, F.G. Will, Parametric study of zinc deposition on porous carbon in a flowing electrolyte cell, J. Electrochem. Soc. 132 (4) (1985) 851–857.
- [44] G. Tomazic, M. Skyllas-Kazacos, Chapter 17 redox flow batteries, in: P.T. Moseley, J. Garche (Eds.), Electrochemical Energy Storage for Renewable Sources And Grid Balancing, Floeyier, Amsterdam, 2015, pp. 309–336.
- Balancing, Elsevier, Amsterdam, 2015, pp. 309–336.
 [45] A. Masliy, N. Poddubny, A.Z. Medvedev, V. Lukyanov, Analysis of the distribution of geometrical current density along the direction of solution flow inside flow-by porous electrodes, J. Electroanal. Chem. 757 (2015) 128–136.
- [46] Y. Qi, T. Jang, V. Ramadesigan, D.T. Schwartz, V.R. Subramanian, Is there a benefit in employing graded electrodes for lithium-ion batteries? J. Electrochem. Soc. 164 (13) (2017) A3196.